

Image deformation in field ion microscopy of faceted crystals

Daniel Niewieczerzał and Czesław Oleksy

Institute of Theoretical Physics, University of Wrocław, Plac Maksa Borna 9, 50-204 Wrocław, Poland

Andrzej Szczepkowicz

Institute of Experimental Physics, University of Wrocław, Plac Maksa Borna 9, 50-204 Wrocław, Poland

(Dated: November 12, 2018)

We perform detailed numerical simulations of field ion microscopy images of faceted crystals and compare them with experimental observations. In contrast to the case of crystals with a smooth surface, for a faceted topography we find extreme deformations of the ion image. Local magnification is highly inhomogeneous and may vary by an order of magnitude: from 0.64 to 6.7. Moreover, the anisotropy of the magnification at a point located on the facet edge may reach a factor of 10.

PACS numbers: 68.37.Vj, 02.70.Dh, 02.70.Ns

I. INTRODUCTION

In recent years field ion microscopy (FIM)^{1,2} has found a number of applications connected with thermally faceted crystals^{3,4}. The most prominent example is the research on the fabrication of atomically sharp electrodes^{5,6,7,8,9,10,11} and their use as practical electron¹² and ion¹³ point sources, including laser-driven femtosecond electron sources^{14,15}. In these studies FIM is often used to determine the electrode shape and the degree of its sharpness. Another example of the application of FIM to faceted crystals is its use in surface science studies of the faceting process itself, in its steplike and global form^{16,17,18}, and in the study of the equilibrium crystal shape¹⁹. Worth mentioning are also FIM studies on single atom diffusion²⁰ – although not carried out on thermally-faceted surfaces, they also encounter the problem of large image distortion at the facet edge.

It is well established that image magnification in FIM is not uniform². This constitutes a problem in the interpretation of the FIM images, and in the past researchers have tried to devise methods which would allow to take into account these effects. Both analytical and numerical calculations of the electric field and ion trajectories have been carried out^{2,21,22}. However, none of these calculations apply to faceted crystals, which are recently most often examined in FIM. Our work is aimed at filling this gap. Faceted crystals, with their atomically sharp edges, produce very large local variations of the intensity and direction of the electric field. This produces huge deflections in ion trajectories, and, consequently, huge distortions in the resulting microscopic image.

In this paper we perform detailed numerical calculations of the ion trajectories in the FIM of faceted crystals. This leads to surprising insights into the interpretation of field ion images of such crystals. Where possible, we confront our numerical results with available experimental data concerning image distortion.

II. METHOD OF CALCULATION

In this section we discuss the numerical approach to simulation of field ion microscope images of faceted surfaces. First, we find the electric field distribution in a model of FIM by solving Laplace's equation, and then the ion trajectories are obtained from classical equations of motion.

A. Construction of the model of a faceted crystal

We will use specimens generated earlier in Monte Carlo simulation of adsorbate-induced faceting on curved surfaces of bcc metal²³. A typical specimen has spherical shape with faceted area around the the [111] pole limited by the inclination angle $\Theta = 20^\circ$. The faceted region of a specimen has a form of a single pyramid with {112} faces or it contains step-like {112} microfacets. We also study truncated pyramids and a pyramid with double edges.

We are especially interested in answering the question how the morphology of faceted surface affects the electric field distribution near the emitter surface. Moreover we want to examine the local magnification on images of faceted surfaces. Thus the FIM model should take into account the atomic roughness of the tip surface and assure long enough distance between the emitter and the screen, or in other words, the model should span many length scales. Such conditions cause big difficulties in numerical solution of Laplace equation on a discrete mesh. On the one hand, the size of the mesh should be equal to the distance between the tip and the screen (~ 10 cm in real experiment). On the other hand, the mesh should have resolution smaller than 1 \AA near the tip. In this paper we demonstrate that solution of Laplace's equation, in a case when the distance between the emitter and the screen is million times larger than the mesh resolution, is possible assuming the following approximations:

- The spherical emitter with faceted region. Atoms in the faceted region are represented by the truncated octahedrons – the Wigner-Seitz cells of the

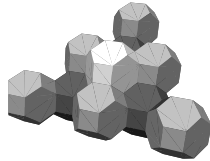


FIG. 1: 3D view of the apex of a pyramid formed of the truncated octahedrons.

bcc crystal structure (see Fig. 1). The remaining part of the emitter is approximated by a smooth sphere of radius R_0 .

- The spherical screen of radius R_1 which is about three hundred times greater than R_0 .

Let us comment the the choice of truncated octahedrons to represent atoms in the FIM model. We considered 3 possibilities: (i) point like atoms and the surface represented by triangles, (ii) hard sphere model, (iii) each atom represented by the truncated octahedron - the Wigner-Seitz cell of a bcc crystal structure. All these cases were preliminarily tested in simulations and we have chosen the representation by truncated octahedrons. The simplest representation by surface triangulation does not accurately reflect the atomic roughness of (111), (211) and (110) faces. The hard sphere model seems to be the best one, but it is difficult to use. If one takes the radius from the close-packed bcc structure, the surface contains plenty of holes between the spheres. On the other hand, choice of larger sphere radius leads to the reduction of the atomic roughness. Representation of atoms by truncated octahedrons ensures that the bcc crystal faces have proper symmetry and atomic roughness, and it is easy to use in numerical calculation.

B. Calculation of the electric field

To calculate the electric field distribution in the FIM model, first one has to solve Laplace's equation (LE) in the space between the emitter and the screen^{21,22}.

$$\Delta V(\mathbf{r}) = 0, \quad (1)$$

where $V(\mathbf{r})$ is the electric potential at the point \mathbf{r} . It is assumed that $V = V_0$ at all points of the emitter surface and the $V = V_1$ at all points of the screen. Then the electric field is obtained:

$$\mathbf{E}(\mathbf{r}) = -\nabla V(\mathbf{r}). \quad (2)$$

To solve LE, Eq. (1), in the space Ω between the emitter and the screen, finite element method (FEM) is applied, because it is well-suited for simulation of geometrically complicated domains^{24,25}. All FEM related calculations are performed using Getfem++ package²⁶, whereas

tetrahedral meshes are generated using TetGen library²⁷. In our application of the finite element method the domain Ω is divided into a number of tetrahedrons and Lagrange-type interpolation functions are used as the basic functions. For such mesh the electric field is constant in a tetrahedron. Hence, to assure appropriate accuracy of \mathbf{E} , especially near the emitter surface, the linear size of a tetrahedron should be much smaller than the lattice constant a . Direct computation does not allow for such mesh refinement, so we overcome this difficulty in the following way. First, we combine the numerical solution of LE with the analytical one. It follows from our preliminary calculation that at distances r from the emitter greater than $5R_0$ the electrostatic potential $V(r)$ for the faceted emitter is practically the same as for the spherical emitter.

It is easy to show that the electrostatic potential V_S for the spherical emitter is given by the formula

$$V_S(r) = \frac{V_1 R_1 - V_0 R_0}{R_1 - R_0} + \frac{(V_0 - V_1) R_0 R_1}{R_1 - R_0} \frac{1}{r} \quad (3)$$

and applying Eq. (2) gives the electric field \mathbf{E}_S

$$\mathbf{E}_S(\mathbf{r}) = \frac{(V_0 - V_1) R_0 R_1}{R_1 - R_0} \frac{\mathbf{r}}{r^3} \quad (4)$$

A numerical solution of LE is limited to a subdomain Ω' of spherical shape with a radius R_{num} . We apply Dirichlet boundary conditions to surfaces in Ω' with $V = V_0$ on internal (emitter) surface and $V = V_S(R_{\text{num}})$ on the external surface. In the space outside the Ω' , i.e., for distance $r > R_{\text{num}}$, the analytical solution given by Eq. (3) and Eq. (4) will be used.

To obtain a numerical solution of LE in the subdomain Ω' with appropriate accuracy for FIM images simulation, we use 3-step procedure described below:

1. The domain Ω' is divided into n spherical layers - subdomains Ω_i , $i = 1, 2, \dots, n$, each with its own mesh of tetrahedrons. Then the LE is solved in the whole Ω' to get values of V on boundaries of each subdomain.
2. In each subdomain Ω_i the LE is solved again on a finer mesh of tetrahedrons applying Dirichlet boundary conditions to Ω_i surfaces where the electric potential is known from solution obtained in the previous step.
3. To calculate the electric field at a point \mathbf{r} within Ω_i :
 - (a) A local subdomain $\omega_{\mathbf{r}}$ is constructed by collecting all tetrahedrons with distance from \mathbf{r} smaller than R_{loc} .
 - (b) A new mesh is created by filling with newly generated tetrahedrons the space inside the $\omega_{\mathbf{r}}$ boundary. There is a special, regular tetrahedron $T_{\mathbf{r}}$ with center located at \mathbf{r}

- (c) Using this mesh, LE is solved imposing V values from the $\omega_{\mathbf{r}}$ boundary as Dirichlet condition.
- (d) Finally, the electric field is obtained as minus gradient of V calculated on $T_{\mathbf{r}}$

Typical technical data used in our calculation: the radius of emitter $R_0 = 268 \text{ \AA}$, assuming the lattice constant for tungsten: $a=3.16 \text{ \AA}$, the radius of Ω' domain $R_{\text{num}} = 33R_0$, the radius of the screen $R_1 = 267R_0$, the number of subdomains $n = 9$, the number of tetrahedrons used in whole Ω' for the 1st step is $N_T = 4728000$ and for the 2nd step in each subdomain Ω_i , $N_T > 2.6 * 10^6$. The size of the special tetrahedron $T_{\mathbf{r}}$ is $\frac{a}{70}$ in the vicinity of emitter surface. Hence, the ratio of R_1 to size of the special tetrahedron is over 10^6 .

It is worth to emphasize an important role of the third step in our procedure of calculating the electric field by using a local subdomain $\omega_{\mathbf{r}}$. Omitting this step leads to an incorrect solution even in Ω_1 subdomain, although Ω_1 has the smallest linear size ($\sim 1.07R_0$) and large number of tetrahedrons in its mesh $N_T = 3.4 * 10^6$.

We performed several tests to verify presented method of solving LE. The most important one concerned calculation of the electric field for an ideal spherical emitter because the analytical solution is known in this case – Eq. (4). The obtained numerical results are in good agreement with analytical solution. In the examined distance range up to $r = 8R_0$, the relative error $|E(r) - E_S(r)|/E_S(r)$ is smaller than $5 * 10^{-4}$ and the deviation of \mathbf{E} direction from the radial direction is smaller than 0.1° . We also obtained positive results for checking the symmetry of the electric field distribution on the different emitter shapes: pyramidal tip and bcc spherical one.

C. Calculation of the ion trajectories

Motion of an ion of mass M and charge q under the influence of force $\mathbf{F}(\mathbf{r}) = q\mathbf{E}(\mathbf{r})$ is described by the equation of motion

$$M \frac{d^2 \mathbf{r}}{dt^2} = q\mathbf{E}(\mathbf{r}). \quad (5)$$

It is assumed that the ion is formed with zero initial velocity at a small distance ($a\frac{\sqrt{3}}{2}$) from a surface atom. It is convenient to express quantities occurring in Eq. (5) in reduced units. Choosing lattice constant a as unit of length, $(V_0 - V_1)/a$ as unit of E and $t_0 = \sqrt{\frac{Ma^2}{q(V_0 - V_1)}}$ as unit of time, the equation of motion Eq. (5) can be expressed in the form

$$\frac{d^2 \tilde{\mathbf{r}}}{d\tilde{t}^2} = \tilde{\mathbf{E}}(\tilde{\mathbf{r}}), \quad (6)$$

where tilde denotes quantity in reduced unit. Thus, the trajectories in reduced units do not depend on the applied

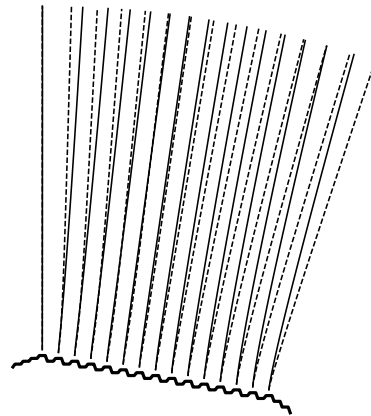


FIG. 2: An example of ion trajectories (continuous lines) and electric field lines (dashed lines) starting from the edge of a pyramid. In this image the length of these lines is limited to $0.5R_0$.

voltage, mass and charge of the ion. These quantities affect unit of time t_0 . To solve Eq. (6) we apply the velocity Verlet algorithm – commonly used in molecular dynamics simulations²⁸, with a time step $0.1t_0$.

It is obvious that the direction of ion trajectory is not coincident with the electric field lines (see Fig. 2) even in the case of the initial ion velocity equal to zero. Due to the curvature of the electric field lines, instantaneous ion velocity at \mathbf{r} is deflected from $\mathbf{E}(\mathbf{r})$ up to large distances from the tip surface.

D. Calculation of a local magnification

Knowing the full ion trajectories we can investigate magnification not only on the distant microscope screen but also on virtual screens at small distances from the emitter. Analysis of FIM images on virtual screens is used to determine the minimal emitter – screen distance. Magnification f is defined here as

$$f = \frac{d'}{d}, \quad (7)$$

where d is the distance of a pair of points on the specimen and d' is the corresponding distance on the screen.

Another important quantity is the local magnification f_l of distance d defined as

$$f_l = \frac{d'}{f_{av} d}, \quad (8)$$

where f_{av} stands for average magnification. The average magnification can be replaced by magnification of a large distance, eg. the distance between ends of pyramid edges.

We found that local magnification of faceted crystal has a long-range dependence on the distance r from the tip. Using the tip with curvature radius $R_0 \approx 27 \text{ nm}$

we obtained that the local magnification reaches 73% of its final value f_l^s at $r = R_0$. At larger distances $f_l(5R_0) \approx 0.9f_l^s$, $f_l(10R_0) \approx 0.94f_l^s$, and $f_l(30R_0) \approx 0.98f_l^s$. Hence, to control the error of f_l , the screen – tip distance in the numerical model should be at least 30 times greater than the tip curvature radius, which is much greater than the distances used in previous numerical studies (see eg.^{21,22}).

III. RESULTS AND DISCUSSION

A. A perfect, single atom pyramid

We begin our calculation with the simple case of a perfect 3-sided pyramid pointing in the $[111]$ direction, formed by three densely packed crystal facets: (211) , (121) , (112) . The crystallographic direction of the pyramid edges is $\langle 311 \rangle$. We assume that all atoms are in the BCC lattice positions and that the pyramid is ended by a single atom. This implies that the number of atoms in the successive (111) planes is $1, 6, 15, 28 \dots$. The assumed sample configuration is shown in Fig. 3(a) and (b). After calculating the resulting electric field $\vec{E}(\vec{r})$ between the sample and the microscope screen, we map the surface atoms onto the microscope screen by following the classical charged-particle trajectories (ions or electrons) – the solution of Eq. 5. The result is shown in Fig. 3(c). The calculated image shows some striking features.

1. Of all the straight lines seen on the sample [Fig. 3(b)], only the pyramid edges remain straight lines on the image [Fig. 3(c)].
2. The magnification of the image is highly inhomogeneous. There is a great enhancement of the magnification at the apex of the pyramid. The local magnification factor at the apex is 4.5.
3. Along the pyramid edge, the local parallel magnification varies from 2.8 near the apex, reaching a minimum (0.64) near the center of the edge (demagnification), increasing to a value of 1.5 near the pyramid base.
4. Along the pyramid edge, the local transverse magnification is 7.4 near the apex, quickly decreasing to a constant value of 6.7.
5. As seen from the comparison of features 3. and 4., the magnification of the image is exceedingly anisotropic – the image is extremely stretched in one direction. In the middle of the pyramid edge, the anisotropy is $6.7/0.64 \sim 10$.

It would be very interesting to confront the above results with experiment. However, there is no easy way to calibrate an FIM image in terms of real distances. It is possible with careful FIM of samples with low average radii, where individual atoms are resolved, but as

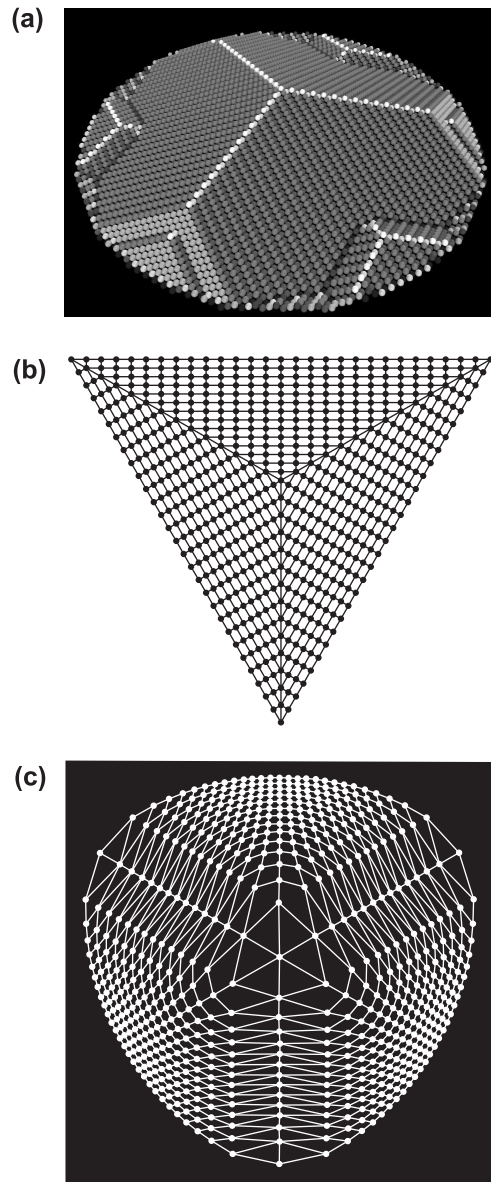


FIG. 3: A single atom pyramid. (a) A three-dimensional visualization of the sample. (b) A projection of the surface atoms of the sample onto a plane. (c) Calculated projection onto the microscope screen following the charged-particle trajectories in the electric field.

the average radius increases, the microscope resolution decreases and one loses the natural reference length of the lattice constant. However, observation 5. appears to explain a peculiar feature of FIM images of pyramids – the images of atoms at the edges are often not circular, but stretched in the direction perpendicular to the edges – see Fig. 4.

The image of atoms shown in Fig. 3(c) does not correspond directly to the experimentally observed FIM image, because in the real microscope only the most protruding atoms are visible. One of the reasons is that the protruding atoms, which can be thought of as “sharp”

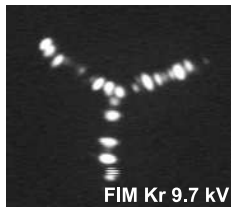


FIG. 4: A FIM image of oxygen-covered tungsten pyramid¹⁹.

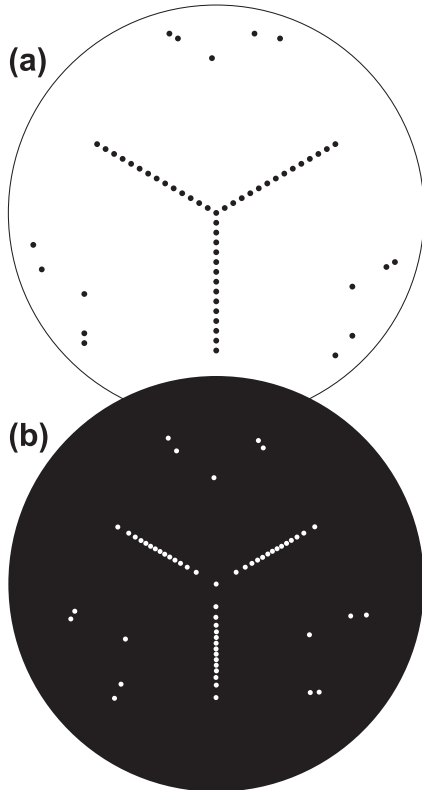


FIG. 5: Atoms which satisfy the ionization criterion (above a threshold field): (a) the sample, (b) the simulated FIM image.

features on the otherwise smooth surface, cause local enhancement in the electric field. Imaging requires field ionization, which takes place for electric field magnitudes exceeding the ionization threshold. Experiments show that for the crystal shape considered here, only the edges of the pyramid are seen in the FIM image. For this reason, for the realistic simulation of the image, we select the atoms where the electric field above the atom exceeds a certain threshold [Fig. 5(a)]. In the last step we calculated the ion trajectories starting from the selected atoms and extending up to the microscope screen to generate a simulated FIM image [Fig. 5(b)].

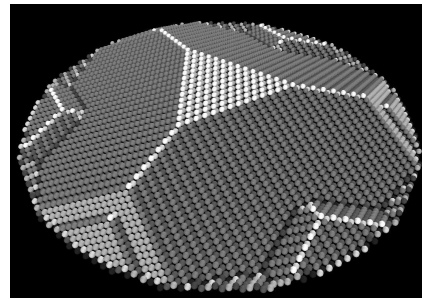


FIG. 6: Visualization of a truncated pyramid (7 atomic (111) layers removed).

B. Truncated pyramids

The exact shape of the $\{211\}$ -faceted crystal can be controlled by careful temperature treatment. It is possible to obtain pyramids with various degrees of vertex truncation or vertex rounding, which can be quantified by measuring the distance d between the pyramid edge end points¹⁹. However, such measurement in FIM suffers from errors caused by the inhomogeneity of the local magnification. If one assumes constant magnification in FIM, the measurements of d are always overestimated – that is, the pyramids are actually more “sharp” than they appear to be in the microscopic image. To calculate the correction for the measurements carried out in¹⁹, we calculated a series of images of truncated pyramids. The height of the single atom pyramid was 14 geometrical atomic layers; now we remove 1,2,3 etc, obtaining an atomic configuration shown in Fig. 6. Three examples of resulting images are shown in Fig. 7. A striking feature is the shape deformation of the truncated vertex area, which has a triangular boundary on the assumed sample, but almost a circular boundary on the simulated image. In FIM experiments, the truncated area is not well resolved, but the boundary of the truncated vertex indeed often appears curved outward, as shown in Fig. 8. As could be expected from the results presented in Sect. III A, the local magnification in the central part of the image is high. For one atomic layer removed, the area of the truncated vertex increases 8.0 times; for 2 layers – 4.8 times; for 5 layers – 2.1 times. The corresponding linear magnifications, proportional to the square roots, are 2.8, 2.2 and 1.4, respectively. As the total height of the pyramid was 14 layers, the local magnifications calculated above correspond to height truncation of 7%, 14% and 36%.

Applying similar considerations as above to the magnification of the distance d between the edge end points, it is possible to correct previous work on the dependence of the equilibrium crystal shape on the temperature¹⁹, as shown in Fig. 9. Note that without the correction based on this work, the amount of truncation of the pyramid is highly overestimated.

In Fig. 10 we demonstrate the simulated image of the (111) surface formed by truncating half of the height of

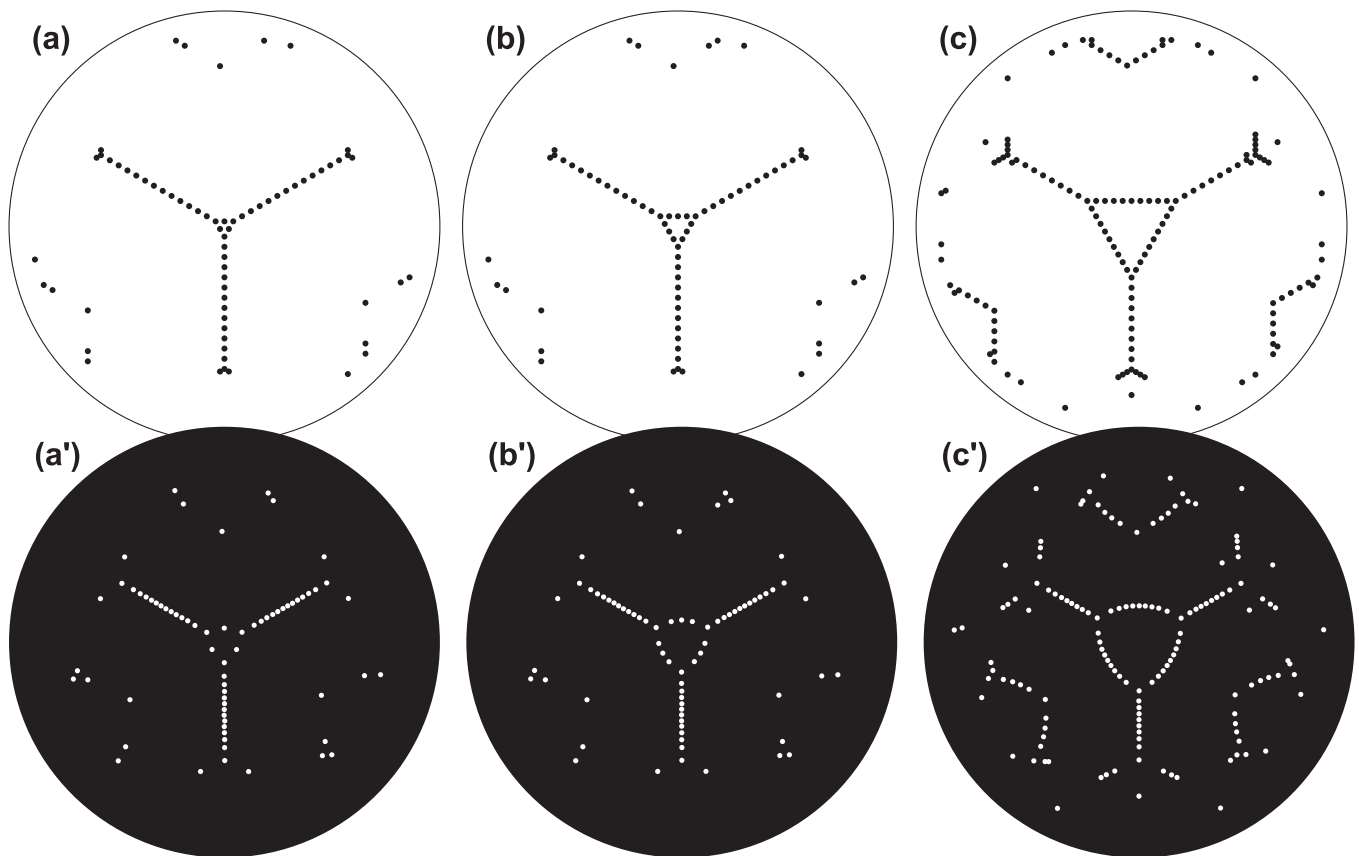


FIG. 7: Truncated pyramids with (a) 1, (b) 2, and (c) 5 atomic layers removed. The corresponding simulated ion images are shown in (a')–(c')

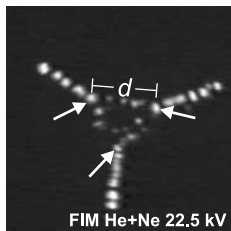


FIG. 8: A FIM image of a truncated pyramid. The arrows point to the edge end points.

the $\{211\}$ pyramid. In the experiment, at this pyramid size the individual atoms would not be resolved; however, in principle all the (111) lattice sites could be visualized using single atom adsorption on the (111) plane, similarly as in the work of Antczak and Ehrlich²⁰. In this way they have observed huge deformations of the image of an atomically flat crystal facet: curving of the atomic lines and an increase of the magnification near the boundary of the facet (Fig. 2 in Ref.²⁰). Both of these features are present in the result of our simulation shown in Fig. 10, further confirming the validity of our model.

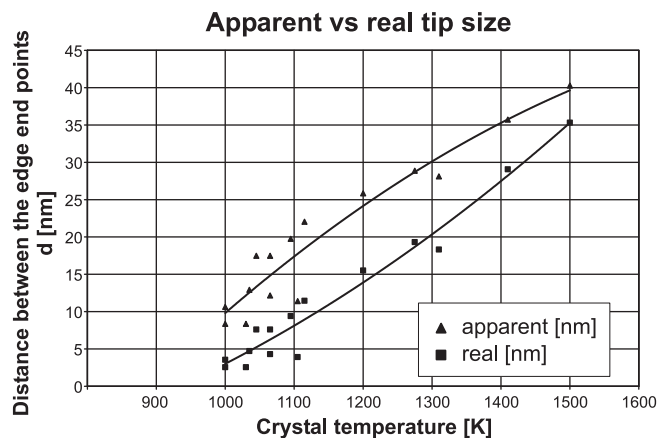


FIG. 9: The corrected dependence of the equilibrium crystal shape on the temperature for oxygen-covered tungsten¹⁹.

C. A steplike-faceted crystal (hill-and-valley faceting)

In the experiment, occurrence of global faceting, where the shape of the faceted crystal is convex, such as described in Sect. III A and III B, is only possible under

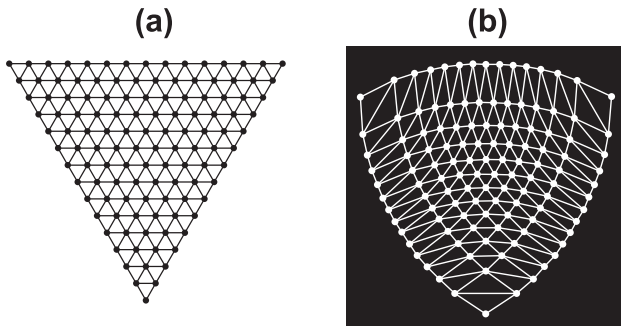


FIG. 10: (a) The atomic arrangement on the (111) plane of the truncated pyramid in Fig. 6. (c) Calculated projection onto the microscope screen following the charged-particle trajectories in the electric field.

special conditions: small crystal, high annealing temperature, and high desorption temperature of the adsorbate. If these conditions are not fulfilled, one obtains a steplike-faceted crystal^{3,18}. This is due to the kinetic limitations on the surface diffusion of the crystal material. For this reason we consider here a steplike-faceted sample, as shown in Fig. 11. The assumed atomic configuration closely corresponds to surface topography observed in the experiments (see e.g. Ref.¹⁷).

Comparison of the simulated and real FIM image [Fig. 11(c) and (d)] shows an overall agreement, but also a discrepancy in one aspect. In the experiment, the six $\langle 311 \rangle$ step edges are not pairwise parallel. One possible reason is that our model sample has a different topography than the real sample near the boundary of the faceted region. Another possibility is that the real atomic configuration is not as perfect as assumed in the calculation [Fig. 11(a)]. Note the high variation of the local magnification along the step edge in the simulated image. Unfortunately, this effect cannot be verified in the real image [Fig. 11(d)] due to the lack of single-atom resolution.

Another atomic configuration, which is interesting for comparison with experiment, is shown in Fig. 12. This is significant for the case of palladium-induced faceting of tungsten^{18,29}. In these experiments, palladium forms a pseudomorphic physical monolayer on the sample. The $\langle 311 \rangle$ edges of pyramids/steps are truncated, with one atomic row removed, as shown in Fig. 12(a). Comparison of the actual atomic arrangement [Fig.12(b)] with the simulated FIM image at the microscope screen [Fig.12(c)] reveals a serious problem in the interpretation of the FIM image in such a case: it is very difficult to infer from the image on the screen [Fig.12(c)] the actual configuration of the atoms [Fig.12(b)]. The image observed on the screen is very misleading, suggesting the presence of three series of four almost equally-spaced parallel edges. This constituted a serious problem in the interpretation of the ion images of Pd/W faceting. Our present calculations finally fully confirm the interpretation of the ion images assumed in previous work^{16,18}, illustrated here in Fig. 13.

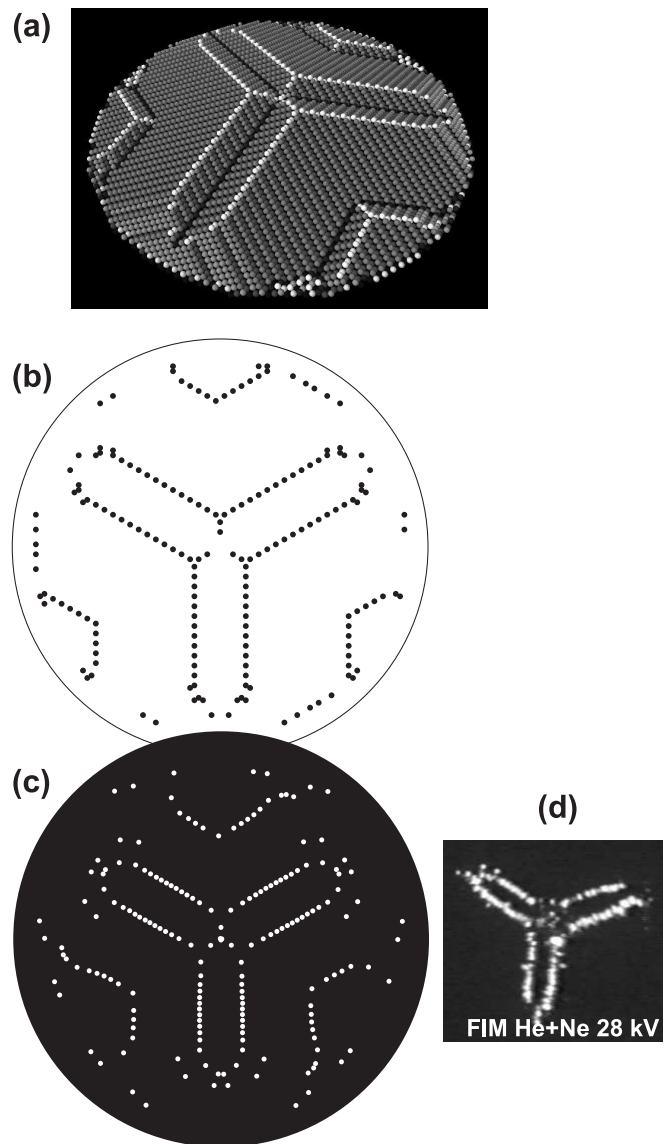


FIG. 11: A steplike-faceted crystal. (a) 3D visualization of the assumed atomic configuration. (b),(c) The positions of the image atoms on the sample and on the screen. (d) Comparison with a real image.

Calculations yield a very large magnification anisotropy: in the middle of the facet edges, the local transverse magnification is 3.1, while the local parallel magnification is 0.74. This results in the image magnification anisotropy of 4.2 at this point – the FIM image is stretched over 4 times in the direction transverse to the facet edges. In the experiment, the local transverse magnification is probably even larger, a rough estimate yields a factor of 7–8 (compare Fig. 13). However, this number is only an estimate, as there is no direct way to measure local magnification in the FIM experiment.

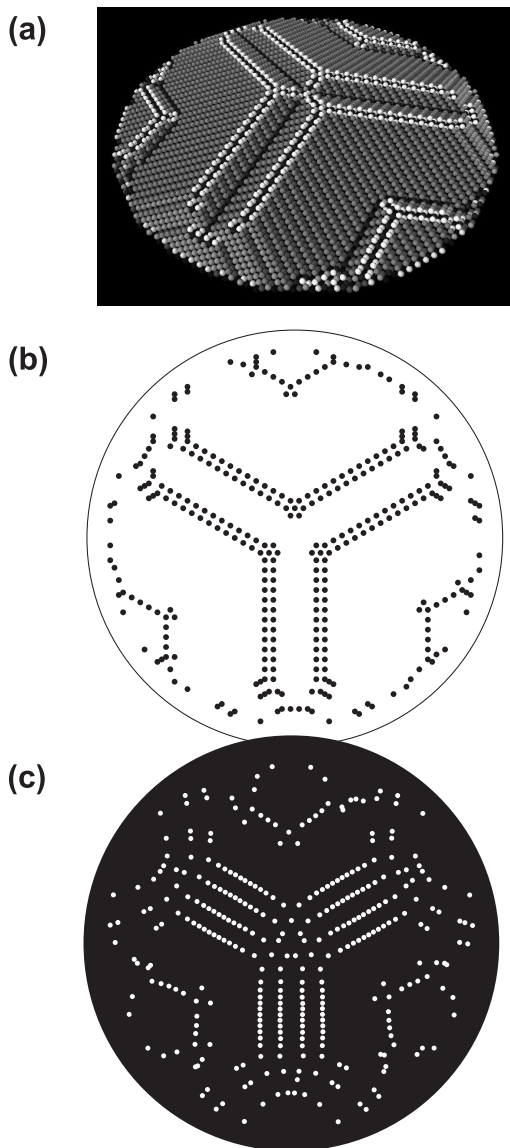


FIG. 12: (a),(b) The assumed atomic configuration and (c) the simulated ion image, corresponding to Pd/W faceting.

IV. CONCLUSION

We performed detailed trajectory calculations in the FIM of $\{211\}$ -faceted crystals (the case often encountered in research), and compared them with available experimental data. We found that the experimentally obtained FIM images of faceted crystals are often very misleading, and one has to rely on numerical calculations to fully account for huge local deformations of the microscopic image. Our main conclusions can be summarised as follows:

1. In the consideration of faceted crystals, it is necessary for the model of FIM to take into account the atomic roughness of the tip surface and, at the same time, the large distance from the tip to the screen

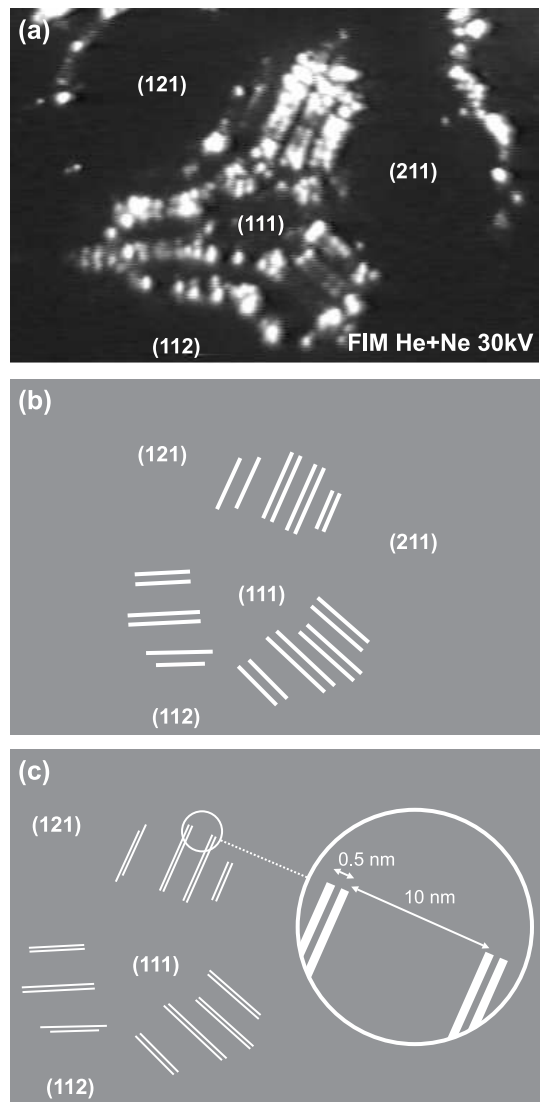


FIG. 13: (a) FIM image of a faceted palladium-covered tungsten surface¹⁸. (b) The position $\{311\}$ edges in image (a). (c) Approximate actual position of the edges on the crystal surface. The distances are estimated from FIM and STM experiments¹⁸.

– the model must span many length scales. Our solution of Laplace’s equation demonstrates that the distance between the tip and the screen in the FIM model should be at least 30 times greater than the tip curvature radius in order to calculate the local magnification correctly.

2. A combination of the finite element method with an analytical solution allows for accurate calculation of the electric field in the space between the tip and the screen.
3. The FIM images of faceted crystals exhibit very large variations of the local magnification. We have found local magnification factors as high as 6.7 and as low as 0.64 (local de-magnification).

4. As one moves along the pyramid or step edge, the parallel magnification varies by a factor of 2–4, reaching a minimum near the middle of an edge.
5. The images of pyramid edges or step edges are exceedingly stretched in the direction perpendicular to the edge. The anisotropy of the local magnification, defined as the ratio of local magnification in two orthogonal directions, reaches a factor of 10 (for a perfect {211} pyramid).
6. As a consequence of 5., an image of a truncated facet edge mimics the image of two distant parallel edges. Great caution is required in the interpretation of this kind of FIM images.
7. The image of a single flat facet is distorted in such

a way that the local magnification increases as one moves toward the facet edge. The atomic rows do not appear straight on the image. Although we have calculated only the case of a (111) facet on top of a {211}-pyramid, comparison with experiment suggests that this conclusion is generally true for isolated flat facets.

8. Truncated {211} pyramids appear significantly more truncated in the FIM image than they are in reality; this effect is most pronounced for small truncations. Numerical calculations are necessary to estimate the size of a {211}-faceted tip.

-
- ¹ T. T. Tsong, *Atom-probe field ion microscopy* (Cambridge University Press, 1990).
 - ² M. K. Miller, A. Cerezo, M. G. Hetherington, and G. D. W. Smith, *Atom Probe Field Ion Microscopy* (Clarendon Press, Oxford, 1996).
 - ³ T. E. Madey, C.-H. Nien, K. Pelhos, J. J. Kolodziej, I. M. Abdelrehim, and H.-S. Tao, *Surf. Sci.* **438**, 191 (1999).
 - ⁴ C.-H. Nien, T. E. Madey, Y. W. Tai, T. C. Leung, J. G. Che, and C. T. Chan, *Phys. Rev. B* **59**, 10335 (1999).
 - ⁵ T.-Y. Fu, L.-C. Cheng, C.-H. Nien, and T. T. Tsong, *Phys. Rev. B* **64**, 113401 (2001).
 - ⁶ A.-S. Lucier, H. Mortensen, Y. Sun, and P. Grütter, *Phys. Rev. B* **72**, 235420 (2005).
 - ⁷ M. Rezeq, J. Pitters, and R. Wolkow, *J. Chem. Phys.* **124**, 204716 (2006).
 - ⁸ R. Bryl and A. Szczepkowicz, *Appl. Surf. Sci.* **252**, 8526 (2006).
 - ⁹ H.-S. Kuo, I.-S. Hwang, T.-Y. Fu, Y.-C. Lin, C.-C. Chang, and T. T. Tsong, *Japanese Journal of Applied Physics* **45**, 8972 (2006).
 - ¹⁰ S. Fujita and H. Shimoyama, *Journal of Vacuum Science and Technology B* **26**, 738 (2008).
 - ¹¹ F. Rahman, J. Onoda, K. Imaizumi, and S. Mizuno, *Surf. Sci.* **602**, 2128 (2008).
 - ¹² C.-C. Chang, H.-S. Kuo, I.-S. Hwang, and T. T. Tsong, *Nanotechnology* **20**, 115401 (2009).
 - ¹³ H.-S. Kuo, I.-S. Hwang, T.-Y. Fu, Y.-H. Lu, C.-Y. Lin, and T. T. Tsong, *Applied Physics Letters* **92**, 063106 (2008).
 - ¹⁴ P. Hommelhoff, Y. Sortais, A. Aghajani-Talesh, and M. A. Kasevich, *Phys. Rev. Lett.* **96**, 077401 (2006).
 - ¹⁵ P. Hommelhoff, C. Kealhofer, A. Aghajani-Talesh, Y. R. P. Sortais, S. M. Foreman, and M. A. Kasevich, *Ultramicroscopy* **109**, 423 (2009).
 - ¹⁶ A. Szczepkowicz and A. Ciszewski, *Surf. Sci.* **515**, 441 (2002).
 - ¹⁷ A. Szczepkowicz and R. Bryl, *Surf. Sci. Lett.* **559**, L169 (2004).
 - ¹⁸ A. Szczepkowicz, A. Ciszewski, R. Bryl, C. Oleksy, C.-H. Nien, Q. Wu, and T. E. Madey, *Surf. Sci.* **599**, 55 (2005).
 - ¹⁹ A. Szczepkowicz and R. Bryl, *Phys. Rev. B* **71**, 113416 (2005).
 - ²⁰ G. Antczak and G. Ehrlich, *Phys. Rev.* **71**, 115422 (2005).
 - ²¹ F. Vurpillot, A. Bostel, and D. Blavette, *Ultramicroscopy* **89**, 137 (2001).
 - ²² F. Vurpillot, A. Cerezo, D. Blavette, and D. Larson, *Microsc. Microanal.* **10**, 384 (2004).
 - ²³ D. Niewieczerzal and C. Oleksy, *Surf. Sci.* **600**, 56 (2006).
 - ²⁴ O.C.Zienkiewicz, R.L.Taylor, and J.Z.Zhu, *Finite Element Method: Its Basis and Fundamentals* (Butterworth Heinemann, Burlington, 2005).
 - ²⁵ S. Rahman, J. Gorman, C. H. W. Barnes, D. A. Williams, and H. P. Langtangen, *Phys. Rev. B* **73**, 233307 (2006).
 - ²⁶ *Getfem++ home page: <http://home.gna.org/getfem>.*
 - ²⁷ *Tetgen home page: <http://tetgen.berlios.de/>.*
 - ²⁸ D. Frenkel and B. Smith, *Understanding Molecular Simulation* (Academic Press, San Diego, 1996).
 - ²⁹ C.-H. Nien and T. E. Madey, *Surf. Sci. Lett.* **380**, L527 (1997).